JOURNAL OF THEORETICAL
AND APPLIED MECHANICS
64, 3, pp. 231–244, Warsaw 2026
https://doi.org/10.15632/jtam-pl/226002

DYNAMIC MODELING OF WIND TURBINE BLADES UNDER UNCERTAINTIES: NONLINEAR ANALYSIS AND STOCHASTIC QUANTIFICATION BY ADVANCED FINITE ELEMENTS

Rania MAKTOUF[1*], Nourhaine YOUSFI[1], Ahmed GHORBEL[2], Nabih FEKI[3], Ali AKROUT[1], Mohamed HADDAR[1]

[1] *Mechanical Modeling and Manufacturing Laboratory (LA2MP), National School of Engineers of Sfax, University of Sfax, Sfax, Tunisia*
[2] *Higher Institute of Applied Sciences and Technology of Kairouan, University of Kairouan, Tunisia*
[3] *Higher Institute of Applied Sciences and Technology of Sousse, University of Sousse, Tunisia*
[*]corresponding author, *raniaphymaktouf@gmail.com*

This article presents a modal and nonlinear dynamic analysis of a twisted blade, highlighting the influence of rotational speed on bending and torsional responses. An advanced finite element formulation is developed, based on separating translational and rotational kinetic energies. The blade is modeled using six-degree-of-freedom beam elements with non-uniform cross-sections, enabling the accurate capture of geometric nonlinearities. Furthermore, the study incorporates the effect of uncertainties in material properties on the dynamic response, combining Monte Carlo simulations and a polynomial chaos approach. The results show that these uncertainties significantly influence displacements, particularly at high rotational speeds, underscoring the importance of robust and probabilistic modeling.

Keywords: wind turbine blade; modal analysis; uncertainty; geometric nonlinearity.

1. Introduction

Rotating beams are key structural elements in many engineering applications, particularly in aerospace and energy systems such as aircraft wings, helicopter rotors, and wind turbine blades (Hodges & Rutkowski, 1981; Jureczko *et al.*, 2005; Leissa *et al.*, 1982). Their dynamic behavior is strongly influenced by rotational speed, which significantly affects natural frequencies and mode shapes (Kim *et al.*, 2013; Park *et al.*, 2010). As a result, accurate vibration analysis is essential for reliable structural design.

Various modeling approaches have been proposed to investigate these systems. The finite element method (FEM) remains the most widely used, enabling detailed evaluation of blade dynamics under centrifugal, gravitational, and gyroscopic effects (Chung & Yoo, 2002; Hamdi *et al.*, 2014). Analytical formulations based on energy methods, particularly Hamilton's principle, have also been developed to describe different vibration modes of rotating beams (Kim *et al.*, 2013). In addition, parametric studies have highlighted the influence of key factors such as rotational speed, tip mass, and geometric characteristics on the overall dynamic response (Lee *et al.*, 2004; Sheibani & Akbari, 2015).

Most early investigations rely on linear assumptions with small deflections (Zhang & Huang, 2011). However, such simplifications are no longer valid for modern large-scale wind turbine blades, which exhibit significant geometric nonlinearities due to their flexibility. To overcome this limitation, several nonlinear formulations have been introduced, although they often involve increased computational cost (Palacios & Cesnik, 2009). Advanced approaches have been proposed to capture large deformation effects with good accuracy, including refined beam theories and nonlinear finite element models (Filippi *et al.*, 2018; Moeenfard & Awtar, 2014; Pagani & Carrera, 2018; Yangui *et al.*, 2018). These studies demonstrate the importance of centrifugal stiffening, damping, and gyroscopic coupling in the dynamic response of rotating structures (Hamdi, 2025; Maktouf *et al.*, 2019).

Despite these advances, uncertainties are often neglected in blade modeling. In practice, turbine blades are subject to variability in material properties, manufacturing processes, and operating conditions. Probabilistic methods provide an appropriate framework to address this issue. The Monte Carlo approach is widely used due to its simplicity, but it requires a high computational cost (Ni *et al.*, 2019). Alternatively, spectral methods such as polynomial chaos expansion (PCE) offer an efficient way to represent uncertainty through orthogonal polynomial bases (Askey & Wilson, 1985). These methods have been successfully applied to structural dynamics, sensitivity analysis, and inverse problems, providing accurate results with reduced computational effort (Ni *et al.*, 2019; Schwarz *et al.*, 2024; Serra & Florentin, 2023). More recently, PCE has been integrated into blade design to account for geometric imperfections and manufacturing variability, improving prediction robustness (Gao *et al.*, 2019; Zhao *et al.*, 2025).

In this context, the present study develops a finite element model of a wind turbine blade to analyze its dynamic behavior under rotation while incorporating uncertainties in material parameters. This combined deterministic-stochastic approach aims to enhance the accuracy and reliability of performance predictions.

2. Numerical modeling and uncertainty

2.1. Blade modeling

The structural design of the turbine blade is illustrated in Fig. 1. The blade structure was modeled using beam elements, each providing six-degrees-of-freedom per node.

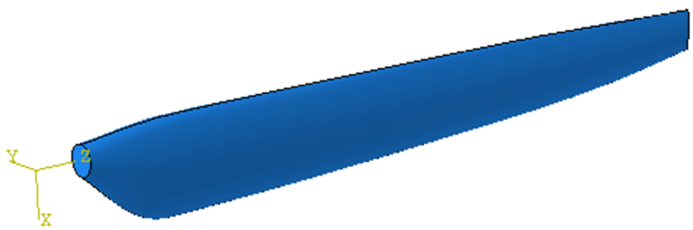

Fig. 1. Wind turbine blade design.

The rotation axis R coincides with the z-axis of the absolute fixed system and Ω_t presents the angular position of the local system with respect to the stationary one.

2.2. Kinetic energy

Let $\{d\}$ denote the motion vector with all blade's degrees of freedom:

$$\{d\} = \{u, v, w, \alpha, \beta, \gamma\}^T. \tag{2.1}$$

The translational displacements along the x-, y-, and z-axes are denoted by u, v, and w, while α, β, and γ represent the corresponding rotations.

The angular velocity vector is defined as

$$\{\Omega\} = \{0 \quad 0 \quad \Omega\}^T. \tag{2.2}$$

The position vector of a point N in the local coordinate system R is

$$\mathbf{r} = \{x, y, z\}^T. \tag{2.3}$$

Using the transformation matrix $[t_m]$, the position in the fixed frame R_1 becomes:

$$\bar{\mathbf{r}}_{R_1} = [t_m]\mathbf{r} = \begin{bmatrix} \cos \Omega t & -\sin \Omega t & 0 \\ \sin \Omega t & \cos \Omega t & 0 \\ 0 & 0 & 1 \end{bmatrix} \begin{Bmatrix} x \\ y \\ z \end{Bmatrix}. \tag{2.4}$$

2.2.1. Translational displacement kinetic energy

The translational motion of a representative point in the local system R, denoted by $\{u_{\text{tran}}\}$ and illustrated in Fig. 2a, is given by

$$\{u_{\text{tran}}\} = \{u \quad v \quad w\}^t. \tag{2.5}$$

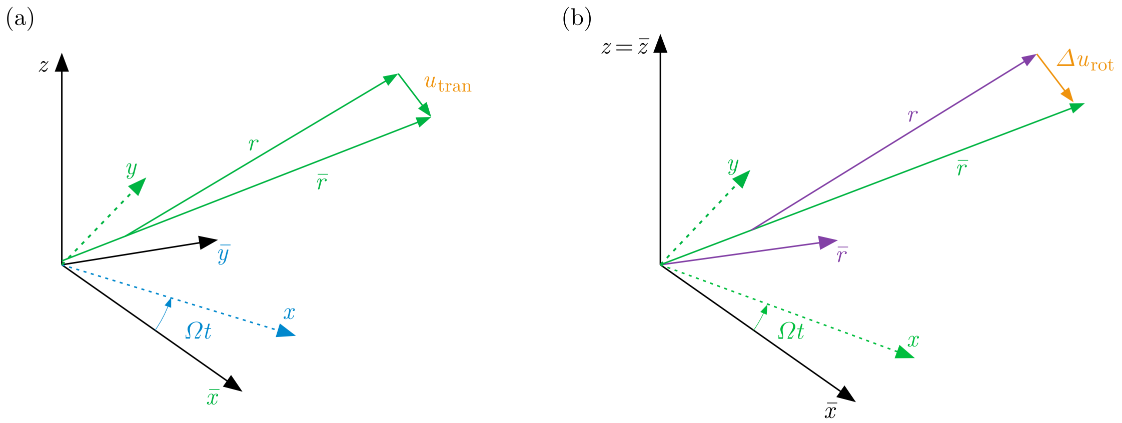

Fig. 2. Blade displacement modes: (a) motion of translational mode; (b) motion of rotational mode.

The kinetic energy in the absolute system R_1 is given by

$$T = \frac{m}{2}\{\dot{\bar{r}}\}^t\{\dot{\bar{r}}\}, \tag{2.6}$$

where the position vector of the locally displaced and globally rotating particle, expressed in the fixed reference frame, is given as follows:

$$\{\bar{r}\} = [t_m](\{r\} + \{u_{\text{tran}}\}). \tag{2.7}$$

The velocity of the vector in Eq. (2.7), expressed in the fixed frame, can be written as follows:

$$\{\dot{\bar{r}}\} = \Omega[\bar{t}_m](\{r\} + \{u_{\text{tran}}\}) + [t_m]\{\dot{u}_{\text{tran}}\}. \tag{2.8}$$

By employing the quantities defined in Eq. (2.8), the kinetic energy takes the following form:

$$T = \frac{m}{2}(\Omega(\{r\}^t + \{u_{\text{tran}}\}^t)[\bar{t}_m]^t + \{\dot{u}_{\text{tran}}\}^t[t_m]^t)(\Omega[\bar{t}_m](\{r\} + \{u_{\text{tran}}\}) + [t_m]\{\dot{u}_{\text{tran}}\}). \tag{2.9}$$

By collecting and arranging the terms, the expression of the kinetic energy of the translational motion was obtained:

$$\begin{aligned} T = {} & \frac{m}{2}(\Omega^2\{r\}^t[J][\{r\}] + 2\Omega^2\{r\}^t[\{J\}]\{u_{\text{tran}}\}) \\ & + \frac{m}{2}(\Omega^2\{u_{\text{tran}}\}^t[\{J\}]\{u_{\text{tran}}\}) + 2\Omega\{\dot{u}_{\text{tran}}\}^t[P]^t[r] \\ & + 2\Omega\{u_{\text{tran}}\}^t[P]\{\dot{u}_{\text{tran}}\} + \{\dot{u}_{\text{tran}}\}^t[I]\{\dot{u}_{\text{tran}}\}), \end{aligned} \tag{2.10}$$

where P denotes the product of the motion and velocity transformation matrix, while J denotes the product of the matrix of velocity transformation and its transpose.

2.2.2. Rotational motion kinetic energy

The vector u_{rot} is defined as the rotational components of the particle along the three nodal axes:

$$\{u_{\mathrm{rot}}\} = \{\alpha \quad \beta \quad \gamma\}^t. \tag{2.11}$$

As a result, the vector Au_{rot} represents the particle's rotational motion induced by the nodal rotation, as illustrated in Fig. 2b.

The moments of inertia can be determined in several ways: by defining a concentrated mass, by distributing the inertia across the finite element mesh among neighboring mass points, or as in our case, by attaching six submasses to the node. This approach corresponds to a lumped-mass approximation, in which the continuous inertia distribution within each element is concentrated at the nodes, neglecting the distributed mass between them. This simplification preserves the translational and rotational nodal inertia associated with the six-degrees-of-freedom and provides a practical compromise between computational efficiency and accuracy for the lower vibration modes considered in this study (Maktouf *et al.*, 2019). In this context, we denote the total mass at the node as $m = 6m'$. The corresponding inertia terms are then expressed as follows:

$$\theta_x = 2m'(y'^2 + z'^2), \qquad \theta_y = 2m'(x'^2 + z'^2), \qquad \theta_z = 2m'(x'^2 + y'^2). \tag{2.12}$$

Here, x', y', z' denote the coordinates of the mass point. Considering a rotation about the z-axis by an angle γ, this induces a transformation of the point's position in the local system, which is described as follows:

$$\{\widetilde{r}\} = \begin{pmatrix} \cos\gamma & -\sin\gamma & 0 \\ \sin\gamma & \cos\gamma & 0 \\ 0 & 0 & 1 \end{pmatrix} \{r\}. \tag{2.13}$$

A rotation about the x-axis by an angle α results in the following transformation:

$$\{\widetilde{r}\} = \begin{pmatrix} 1 & 0 & 0 \\ 0 & \cos\alpha & -\sin\alpha \\ 0 & \sin\alpha & \cos\alpha \end{pmatrix} \{r\}. \tag{2.14}$$

Finally, a rotation about the y-axis by an angle β yields the following transformation:

$$\{\widetilde{r}\} = \begin{pmatrix} \cos\beta & 0 & \sin\beta \\ 0 & 1 & 0 \\ -\sin\beta & 0 & \cos\beta \end{pmatrix} \{r\}. \tag{2.15}$$

The combined transformation is obtained by multiplying the three preceding matrices and can be expressed as follows:

$$\{\widetilde{r}\} = ([I] + [\widetilde{A}])\{r\}, \tag{2.16}$$

where

$$[\widetilde{A}] = \begin{pmatrix} 0 & -\gamma & \beta \\ \gamma & 0 & -\alpha \\ -\beta & \alpha & 0 \end{pmatrix}. \tag{2.17}$$

The nodal rotations can be converted into nodal translations using the following relation:

$$\{Au_{\mathrm{rot}}\} = [A]\{u_{\mathrm{rot}}\} = [A]\{\alpha, \beta, \gamma\}^T, \tag{2.18}$$

where

$$[A] = \begin{pmatrix} 0 & z' & -y' \\ -z' & 0 & x' \\ y' & -x' & 0 \end{pmatrix}. \tag{2.19}$$

By applying Eqs. (2.6) and (2.7) for the rotational displacement, the position vector in the fixed system can be expressed as follows:

$$\overline{\{r\}} = [t_m]\{r\} + [t_m][A]\{u_{\rm rot}\}. \tag{2.20}$$

By differentiating the preceding equation, the velocity can be expressed as

$$\overline{\{\dot r\}} = \Omega[t_m]\{r\} + \Omega\overline{[t_m]}[A]\{u_{\rm rot}\} + [t_m][A]\{\dot u_{\rm rot}\}. \tag{2.21}$$

Following the same procedure applied to translational displacement, the kinetic energy associated with rotational motion is given by:

$$\begin{aligned} T = {} & \frac{m}{2}(\Omega^2\{r\}^t[J]\{r\} + 2\Omega^2\{r\}^t[J][A]\{u_{\rm rot}\} + 2\Omega\{r\}^t[P][A]\{u_{\rm rot}\}) \\ & + \frac{m}{2}(\Omega^2\{u_{\rm rot}\}^t[A]^t[J][A]\{u_{\rm rot}\} + 2\Omega\{u_{\rm rot}\}^t[A]^t[P][A]\{u_{\rm rot}\}) \\ & + \frac{m}{2}(\{u_{\rm rot}\}^t[A]^t[I][A]\{u_{\rm rot}\}). \end{aligned} \tag{2.22}$$

2.3. Equations governing motion

The stiffness matrix is obtained by integrating the deformation matrix $[B]$ with the matrix of elastic stiffness $[\widetilde{E}]$ (Batoz & Dhatt, 1990):

$$[K_e] = \int\limits_V [B]^t[\widetilde{E}][B], \tag{2.23}$$

$$[\widetilde{E}] = \frac{E}{(1+\nu)(1-2\nu)}\begin{pmatrix} \mathbf{D} & \mathbf{0} \\ \mathbf{0} & \dfrac{1-2\nu}{2}\mathbf{I}_3 \end{pmatrix}, \qquad \mathbf{D} = \begin{pmatrix} 1-\nu & \nu & \nu \\ \nu & 1-\nu & \nu \\ \nu & \nu & 1-\nu \end{pmatrix}, \tag{2.24}$$

where $[\widetilde{E}]$ denotes the elasticity matrix, E is the elastic modulus, $[B]$ is the deformation matrix, and ν is Poisson's ratio. Applying Lagrange's equation of motion to the kinetic energy of translational motion yields:

$$\frac{d}{dt}\left(\frac{\partial T}{\partial\{\dot u_{\rm tran}\}}\right) - \frac{\partial T}{\partial\{u_{\rm tran}\}} = 0. \tag{2.25}$$

Considering that $[P]^t = -[P]$, we obtain:

$$m[I]\{\ddot u_{\rm tran}\} + 2\Omega m[P]\{\dot u_{\rm tran}\} - \Omega^2 m[I]\{u_{\rm tran}\} = \Omega^2 m[J]\{r\}, \tag{2.26}$$

where $\Omega^2 m[J]\{r\}$ represents the centrifugal force. As shown in Eq. (2.28), this force depends on the particle's radial position and the rotational speed:

$$m\Omega^2[J]\{r\} = \{f_{\rm ctran}\}. \tag{2.27}$$

We introduce new matrices associated with the translational motion: $[M_{\mathrm{tran}}]$, $[C_{\mathrm{tran}}]$, and $[Z_{\mathrm{tran}}]$, which represent the element mass, gyroscopic, and centrifugal stiffness matrices, respectively,

$$[M_{\mathrm{tran}}] = m[I] = \begin{bmatrix} m & 0 & 0 \\ 0 & m & 0 \\ 0 & 0 & m \end{bmatrix}, \tag{2.28}$$

$$[C_{\mathrm{tran}}] = m[P] = \begin{bmatrix} 0 & -m & 0 \\ m & 0 & 0 \\ 0 & 0 & 0 \end{bmatrix}, \tag{2.29}$$

$$[Z_{\mathrm{tran}}] = m[J] = \begin{bmatrix} m & 0 & 0 \\ 0 & m & 0 \\ 0 & 0 & 0 \end{bmatrix}. \tag{2.30}$$

Considering only the kinetic energy associated with translational displacement, the matrix equation of motion takes the form:

$$[M_{\mathrm{tran}}]\{\ddot{u}_{\mathrm{tran}}\} + 2\Omega[C_{\mathrm{tran}}]\{\dot{u}_{\mathrm{tran}}\} - \Omega^2[Z_{\mathrm{tran}}]\{u_{\mathrm{tran}}\} = \{f_{\mathrm{tran}}\}. \tag{2.31}$$

Applying Lagrange's equation of motion to the vector of rotation u_{rot} yields:

$$\frac{d}{dt}\left(\frac{\partial T}{\partial\{\dot{u}_{\mathrm{rot}}\}}\right) - \frac{\partial T}{\partial\{u_{\mathrm{rot}}\}} = [M_{\mathrm{rot}}]\{\ddot{u}_{\mathrm{rot}}\} + 2\Omega[C_{\mathrm{rot}}]\{\dot{u}_{\mathrm{rot}}\} - \Omega^2[Z_{\mathrm{rot}}]\{u_{\mathrm{rot}}\} = \{f_{crot}\}, \tag{2.32}$$

where $[M_{\mathrm{rot}}]$ is the mass matrix, $[Z_{\mathrm{rot}}]$ is the centrifugal stiffness matrix, $[C_{\mathrm{rot}}]$ is the gyroscopic matrix, and $\{f_{\mathrm{crot}}\}$ is the centrifugal force vector:

$$[M_{\mathrm{rot}}] = \begin{bmatrix} \theta_x & 0 & 0 \\ 0 & \theta_y & 0 \\ 0 & 0 & \theta_z \end{bmatrix}, \tag{2.33}$$

$$[C_{\mathrm{rot}}] = \begin{bmatrix} 0 & -\frac{1}{2}(\theta_x + \theta_y - \theta_z) & 0 \\ \frac{1}{2}(\theta_x + \theta_y - \theta_z) & 0 & 0 \\ 0 & 0 & 0 \end{bmatrix}, \tag{2.34}$$

$$[Z_{\mathrm{rot}}] = \begin{bmatrix} (\theta_y - \theta_z) & 0 & 0 \\ 0 & (\theta_x - \theta_z) & 0 \\ 0 & 0 & 0 \end{bmatrix}, \tag{2.35}$$

$$\{f_{\mathrm{crot}}\} = m\Omega^2\{-z'y' \quad z'x' \quad 0\}^t. \tag{2.36}$$

The blade displacement induces additional strain energy under rotation, resulting in a geometric stiffness matrix as

$$[K_g] = \int\limits_V [G]^t[\sigma][G]dV, \tag{2.37}$$

where $[G]$ is the matrix relating the nodal motions to their derivatives, and $[g]$ is the stress matrix expressed as

$$[g] = \begin{bmatrix} [S] & 0 & 0 \\ 0 & [S] & 0 \\ 0 & 0 & [S] \end{bmatrix}, \tag{2.38}$$

where

$$[S] = \begin{bmatrix} \sigma_x & \tau_{xy} & \tau_{xz} \\ \tau_{xy} & \sigma_y & \tau_{yz} \\ \tau_{xz} & \tau_{yz} & \sigma_z \end{bmatrix}. \tag{2.39}$$

Finally, the nonlinear equation of motion can be expressed as

$$[M]\{\ddot{q}\} + [C]\{\dot{q}\} + ([K_E] + [K_R] + [K_G])\{q\} = \{F\}. \tag{2.40}$$

Here, the global matrices $[M]$, $[C]$, $[K_E]$, $[K_R]$, $[K_G]$, and the force vector $\{F\}$ are assembled from the element matrices.

All were obtained by assembling the element matrices defined as follows:

$$[M_e] = \begin{bmatrix} [M_{\mathrm{tran}}] & 0 \\ 0 & [M_{\mathrm{rot}}] \end{bmatrix}, \tag{2.41}$$

$$[K_r] = -\Omega^2 \begin{bmatrix} [Z_{\mathrm{tran}}] & 0 \\ 0 & [Z_{\mathrm{rot}}] \end{bmatrix}, \tag{2.42}$$

$$[C_e] = 2\Omega \begin{bmatrix} [C_{\mathrm{tran}}] & 0 \\ 0 & [C_{\mathrm{rot}}] \end{bmatrix}, \tag{2.43}$$

$$\{F_e\} = \begin{Bmatrix} f_{\mathrm{ctran}} \\ f_{\mathrm{crot}} \end{Bmatrix}. \tag{2.44}$$

2.4. Uncertainty quantification methods

Uncertainty propagation is performed using both Monte Carlo simulation and generalized polynomial chaos (GPC). Monte Carlo is used as a reference solution, while GPC is adopted for its high computational efficiency.

2.4.1. Monte Carlo method

The Monte Carlo method estimates output statistics through random sampling of uncertain inputs. For a model $y = f(\mathbf{r})$, the expectation is approximated by

$$\mathbb{E}[y] \approx \frac{1}{N}\sum_{i=1}^{N} f(\mathbf{r}_i), \tag{2.45}$$

where $\mathbf{r}_i$ is the independent sample and N denotes the number of realizations. Although accurate, this method requires a large number of simulations, resulting in high computational cost.

2.4.2. Generalized polynomial chaos method

The GPC method represents the model response as a spectral expansion:

$$y(\boldsymbol{\xi}) \approx \sum_{k=0}^{P} c_k \Phi_k(\boldsymbol{\xi}), \tag{2.46}$$

where P is the order of the expansion and Φ_k are orthogonal polynomials satisfying:

$$\mathbb{E}[\Phi_i \Phi_j] = \delta_{ij}\langle \Phi_j^2 \rangle. \tag{2.47}$$

The polynomial basis is selected according to the Askey scheme (Askey & Wilson, 1985), such as Hermite (Gaussian), Legendre (uniform), Laguerre (gamma), and Jacobi (beta). The GPC implementation adopted in this study is non-intrusive, treating the deterministic finite element solver as a black box. The stochastic modes are determined by a regression-based least-squares solution at Gauss–Legendre collocation points. The uncertain parameters E and G_t are modeled as uniform random variables bounded within $\pm 5\,\%$ and $\pm 20\,\%$ of their nominal values, and the Legendre polynomial basis is adopted consistent with the Askey scheme (Askey & Wilson, 1985). A second-order expansion ($p = 2$) is retained, whose accuracy is confirmed by the excellent agreement with the Monte Carlo reference solution across all investigated configurations (Fig. 6 to Fig. 8). Figure 3 illustrates the overall methodology used in this study.

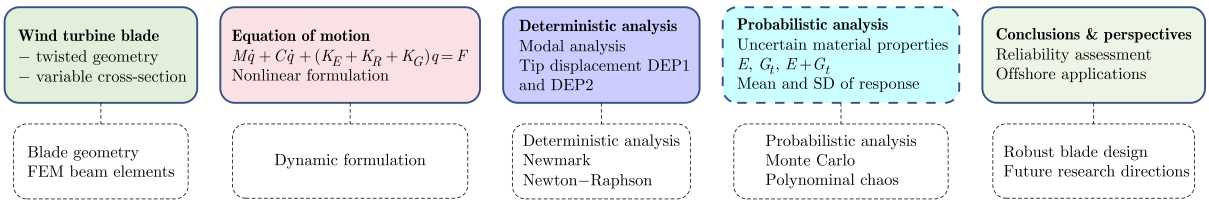

Fig. 3. Flowchart used to study the wind turbine blade under uncertainty.

3. Numerical results

The numerical simulation carried out in MATLAB begins with the determination of the displacement responses. The Monte Carlo and the polynomial chaos methods are then applied to extract the average values of these responses, based on the standard deviations (SDs) of the defined uncertain parameters. The blade material parameters are summarized in Table 1.

Table 1. Material parameters of the turbine blade.

Density ρ [Kg/m^3]	2700
Young modulus E [N/m^2]	6.9×10^{10}
Shear modulus G_t [N/m^2]	2.7×10^{10}
Poisson's ratio ν	0.33

3.1. Dynamic behavior of the deterministic model

The modal analysis is performed for the non-rotating case ($\Omega = 0$), for which all rotation-dependent matrices reduce to zero and the equation of motion reduces to the standard eigenvalue problem $\big([\mathbf{K}_E] - \omega^2[\mathbf{M}]\big)\,\{\varphi\} = \{0\}$. The proposed finite element model was validated by comparing the first five natural frequencies and their associated modal shapes with the results obtained using ABAQUS V6.16. Quantitative validation is presented in Table 2, while Fig. 4 illustrates the corresponding eigenmodes. Good agreement is observed between the two models, with small relative differences, confirming the ability of the developed model to accurately reproduce the dynamic behavior of the blade.

Table 2. Comparison of natural frequencies predicted by the present model and ABAQUS.

Mode	Present model [Hz]	ABAQUS [Hz]	Error [%]
1	6.50	6.30	3.17
2	13.70	12.60	8.1
3	23.00	22.40	2.68
4	53.80	52.15	3.16
5	64.30	65.50	1.8

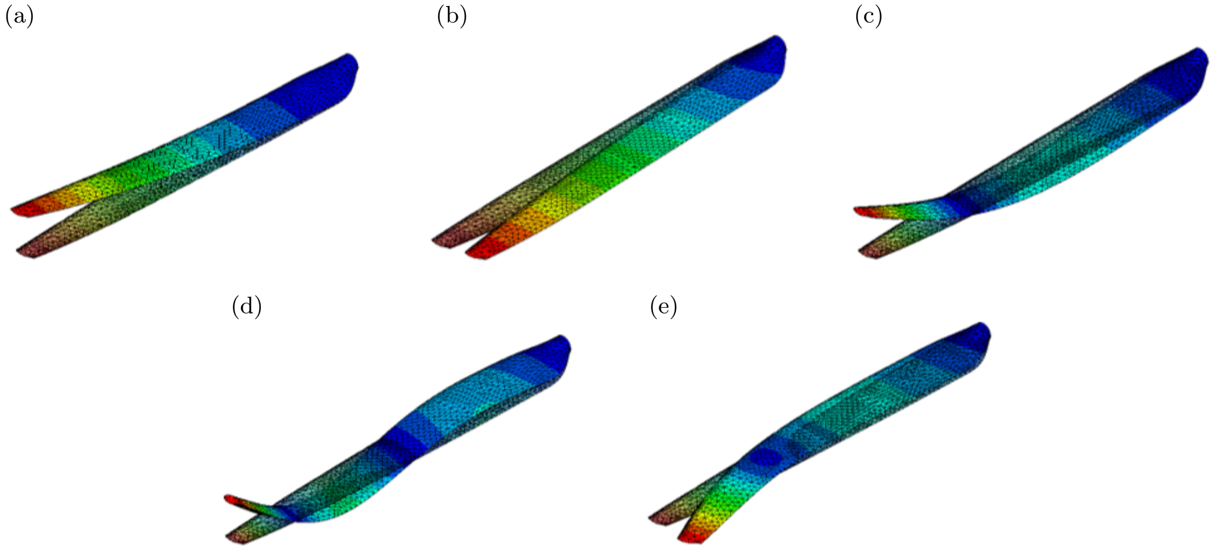

Fig. 4. Initial set of natural frequencies for the blade obtained using Abaqus software: (a) flapwise deflection (6.301 Hz); (b) edgewise deflection (12.601 Hz); (c) flapwise deflection (22.403 Hz); (d) flapwise deflection (52.146 Hz); (e) edgewise deflection (65.547 Hz).

Furthermore, the deterministic displacement responses at the blade tip are presented in Fig. 5 for the flapwise and edgewise directions. These results highlight the expected nonlinear effects on the dynamic response and form the basis of the uncertainty analysis developed in the remainder of the study. Here, the blade tip displacement (DEP1, DEP2) refers to the stabilized tip deflection value reached at equilibrium for a given rotational frequency, obtained from the deterministic model, and constitutes the quantity propagated through the uncertainty quantification framework.

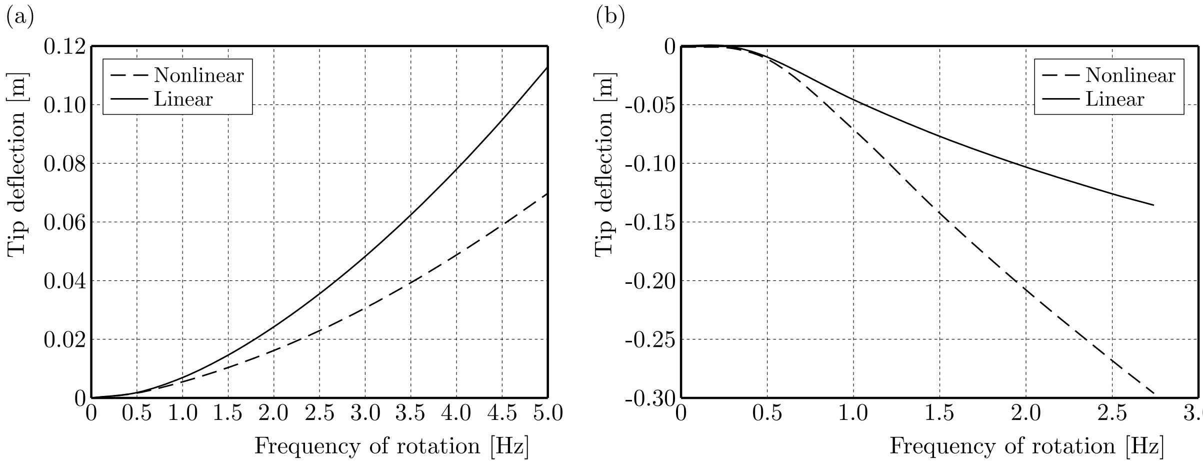

Fig. 5. Tip blade displacement in flapwise (a) and edgwise (b) directions.

3.2. Probabilistic simulations of wind turbine blade

For the upcoming simulations, uncertainty quantification methods will be applied to assess the system's dynamic behavior under variations in the material parameters. During the design process, several material variables may influence the system. In this study, Young's modulus E and the shear modulus G_t are uncertain with SDs equal to 5 % and 20 %, so as to evaluate their impact on the dynamic response of the blade. The simulations follow the framework of the uncertainty study shown in Section 3. In the first stage, uncertainty was introduced through a single uncertainty parameter (uncoupled form) and after that a coupled form was studied in order to show the effect of uncertainty in the blade displacements.

3.2.1. Effect of Young's modulus E

The first simulation focuses on the uncertainty of Young's modulus E with an SD σ_E equal to 5 % and 20 %.

Figure 6 shows the mean value and SD of the displacements in the flapwise (DEP1) and edgewise (DEP2) directions, obtained using the Monte Carlo and GPC approaches for two levels of uncertainty of Young's modulus E: $\sigma_E = 5\,\%$ and $20\,\%$. Figure 6a and Fig. 6b show that the mean values of the flapwise (DEP1) and edgewise (DEP2) displacements increase progressively with the rotational frequency. Increasing σ_E from 5 % to 20 % induces only a slight variation in the mean, indicating that uncertainties in E have a weak influence on the central tendency of the blade's dynamic behavior. The results obtained by the GPC method are in excellent agreement with those from the Monte Carlo simulation, thus confirming the validity and accuracy of the second-order polynomial expansion ($p = 2$) for estimating the mean response of the system.

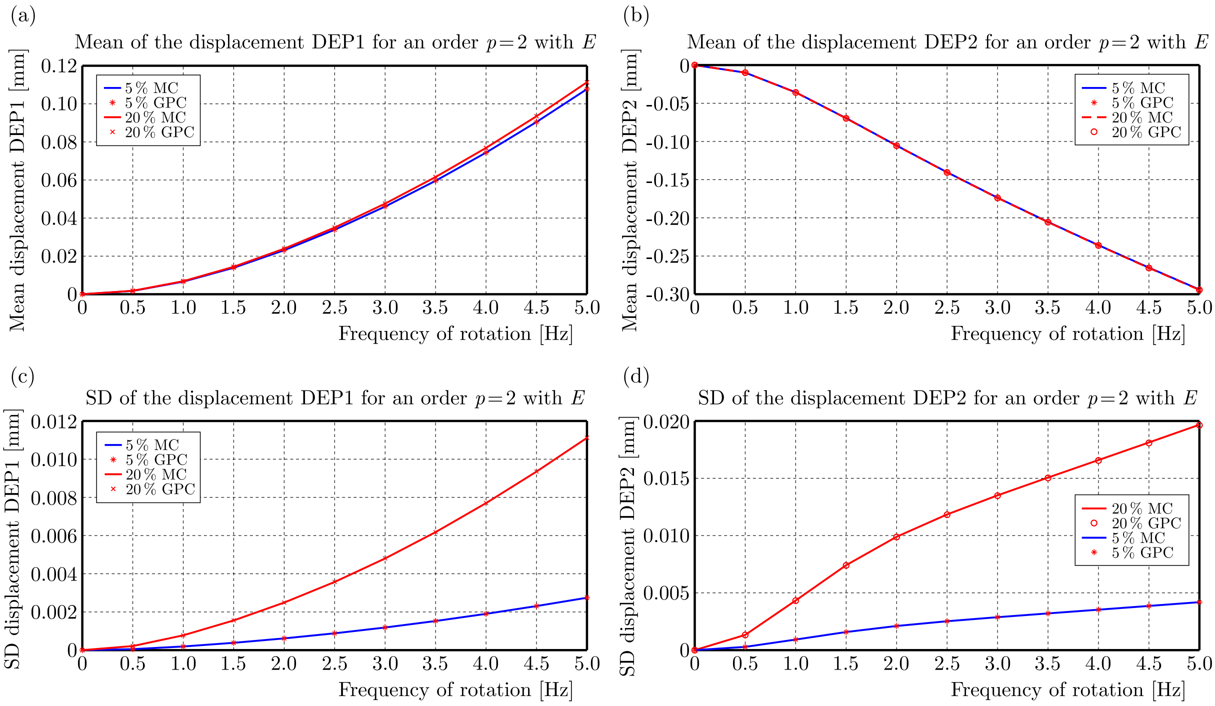

Fig. 6. Mean value and SD of the displacement for DEP1 and DEP2 with $\sigma_E = 5\,\%$ and $20\,\%$.

In the case of the flapwise displacement (DEP1), the response remains positive and increases with the frequency, reflecting increased deflection in the blade's principal plane. Conversely, the edgewise displacement (DEP2) is negative and decreases with frequency, which reflects a bending opposite to the direction of rotation, dominated by inertial and aerodynamic forces.

The results highlight the sensitivity of the responses to uncertainties in Young's modulus. The increase in input variance ($\sigma_E = 20\,\%$) strongly amplifies the SD of the displacements for both deflection directions. This amplification is particularly pronounced at high frequencies, emphasizing that the effects of material uncertainties become more significant in fast dynamic regimes. The GPC curves faithfully reproduce the Monte Carlo results, while considerably reducing the computational cost, confirming the reliability of the polynomial probabilistic framework for quantifying uncertainties in vibration responses DEP1 and DEP2 in the presence of E.

3.2.2. Effect of the shear modulus G_t

The next simulation focuses on the uncertainty in the shear modulus G_t, with the SD σ_{G_t} set to 5 % and 20 %. Figure 7 presents the evolution of the mean value and SD of the flapwise (DEP1)

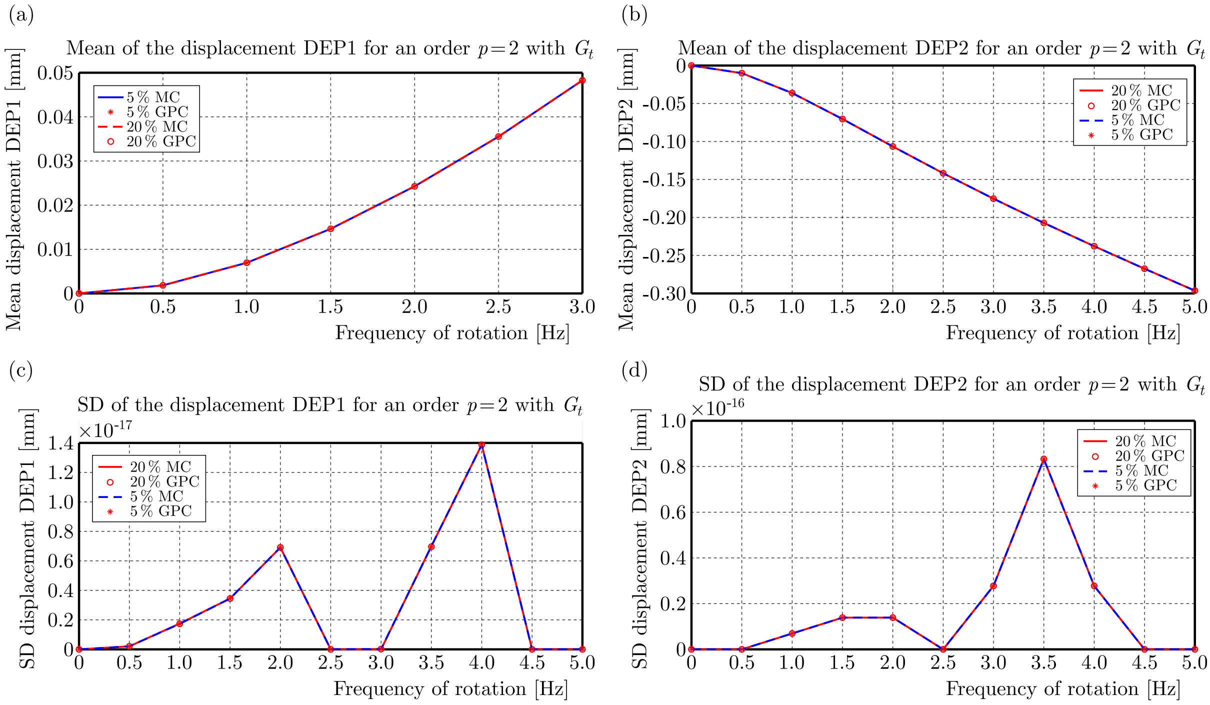

Fig. 7. Mean value and SD of blade tip displacements (DEP1 and DEP2) for $\sigma_{G_t} = 5\,\%$ and $20\,\%$.

and edgewise (DEP2) displacements for the two uncertainty levels. The obtained results indicate that the average displacements DEP1 and DEP2 remain virtually identical for both uncertainty levels of G_t. Also, the GPC results perfectly reproduce those of the Monte Carlo simulation. This superposition of the curves indicates that, unlike E, the variability of the shear modulus G_t has little influence on the average value of the deflections in both directions.

From a physical perspective, this is explained by the fact that G_t primarily governs the torsional stresses and shear deformations of the blade profile. Under the conditions considered here, the flapwise and edgewise bending behavior is dominated by the contributions of Young's modulus E. Therefore, the perturbation of G_t only marginally affects the overall stiffness. Thus, the average response of the blade remains essentially unchanged, whether the dispersion of G_t is moderate ($5\,\%$) or high ($20\,\%$). The observed behavior reflects the weak coupling between torsion and bending under the considered loading conditions. Specifically:

– the flapwise displacement (DEP1) depends primarily on the longitudinal bending stiffness dominated by E;
– the edgewise displacement (DEP2), although influenced by shear effects, remains strongly constrained by axial stiffness and inertial forces, limiting the direct effect of G_t.

3.2.3. Effect of coupled uncertainty

In this part, we study the effect of coupled uncertainty $E + G_t$ in the response of the wind turbine blade. Figure 8 shows the mean value and SD of the flapwise (DEP1) and edgewise (DEP2) displacements for $\sigma_{E+G_t} = 5\,\%$ and $20\,\%$.

The results illustrated in Fig. 8 indicate that increasing the uncertainty level from $5\,\%$ to $20\,\%$ in both E and G_t has a limited effect on the mean displacements in both flapwise (DEP1) and edgewise (DEP2) directions. This behavior highlights the relatively high structural stiffness of the blade, for which moderate variations in material properties do not significantly alter the average response.

Regarding variability, the SD increases proportionally with the uncertainty level, indicating an almost linear propagation of input uncertainties. At low rotational frequencies, the response

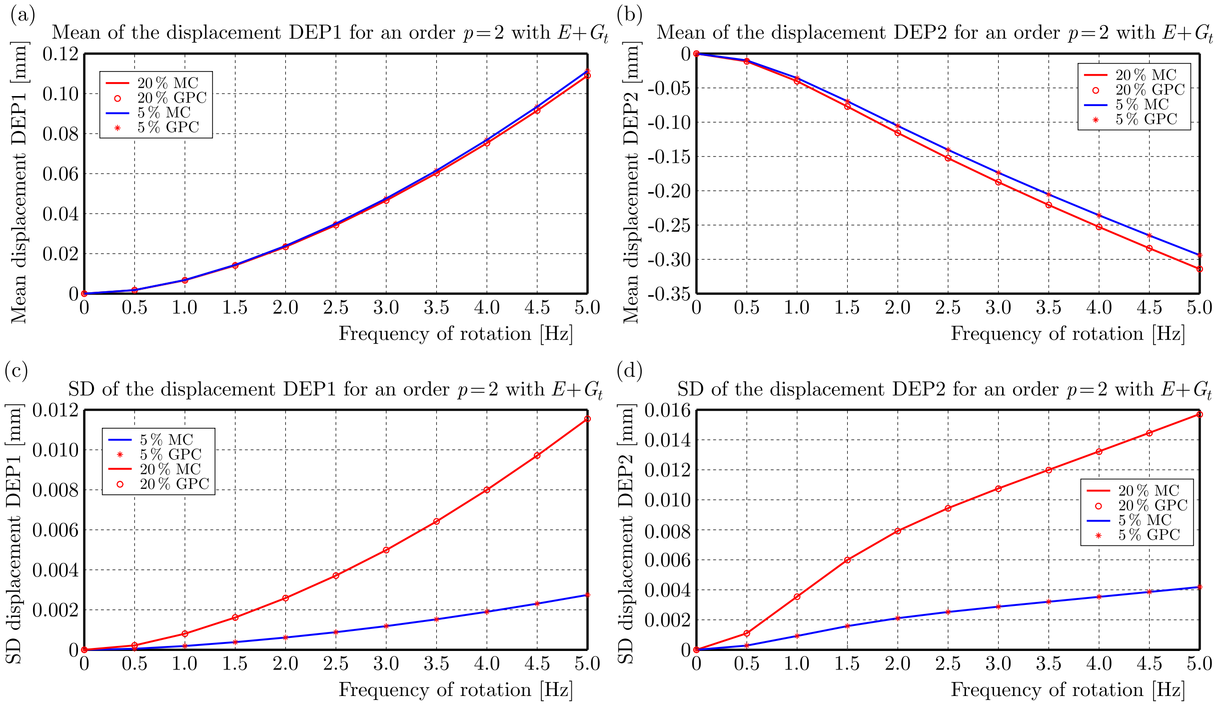

Fig. 8. Mean value and SD of blade tip displacements (DEP1 and DEP2) for combined uncertainties $\sigma_{E+G_t} = 5\,\%$ and $20\,\%$.

remains nearly deterministic, whereas at higher frequencies, the variability is amplified due to inertial effects. This amplification suggests that material uncertainties may play a more significant role under dynamic operating conditions, potentially influencing long-term fatigue behavior.

Overall, the results demonstrate that while the mean response is weakly affected by material variability, the dispersion of the dynamic response becomes more pronounced at higher excitation levels, underlining the importance of uncertainty quantification for reliable blade design.

4. Conclusion

This article introduces a novel finite element model for rotating wind turbine blades, grounded in beam theory and incorporating critical geometric nonlinearities often neglected in conventional approaches. The blade motion equation was resolved by coupling the Newmark time-integration procedure with a Newton–Raphson iterative algorithm to compute the displacement criterion used for stability assessment, which allows the extraction of displacement responses. Moreover, flapwise and edgewise deflections on the tip of the blade have been obtained. A thorough comparison between Monte Carlo simulation and GPC highlights their respective strengths for quantifying material uncertainties: the robustness of Monte Carlo in the face of complex distributions, offset by its slow convergence, versus the computational efficiency of GPC for moderate-dimensional problems. For the adopted numerical settings (Monte Carlo with 1000 samples), the polynomial chaos approach required approximately 90 times less computational time than the Monte Carlo simulation, while providing comparable estimates of the statistical moments. This comparison reflects computational efficiency rather than a formal convergence-rate analysis. In short, this study demonstrates the originality of a holistic integration between nonlinear dynamics and probabilistic uncertainty quantification, essential for boosting the durability and performance of wind turbines. It provides new perspectives for offshore applications, where the incorporation of nonlinearities associated with dynamic loads or extreme conditions could further improve these predictions, motivating future research on AI-based real-time optimization.

References

1. Askey, R., & Wilson, J. (1985). Some basic hypergeometric orthogonal polynomials that generalize Jacobi polynomials. *Memoirs of the American Mathematical Society*, *54*(319). https://doi.org/10.1090/memo/0319

2. Batoz, J.-L., & Dhat, G. (1990). *Finite element modeling of structures. Vol. 1: Elastic solids* (in French). Presses de l'Université Laval.

3. Chung, J., & Yoo, H.H. (2002). Dynamic analysis of a rotating cantilever beam by using the finite element method. *Journal of Sound and Vibration*, *249*(1), 147–164. https://doi.org/10.1006/jsvi.2001.3856.

4. Filippi, M., Pagani, A., & Carrera, E. (2018). Accurate nonlinear dynamics and mode aberration of rotating blades. *Journal of Applied Mechanics*, *85*(11), Article 111004. https://doi.org/10.1115/1.4040693.

5. Gao, L., Ma, C., & Cai, Y. (2019). A robust blade design method based on non-intrusive polynomial chaos considering profile error. *Journal of Thermal Science*, *28*(5), 875–885. https://doi.org/10.1007/s11630-019-1185-6.

6. Hamdi, H. (2025). Three-dimensional linear vibration of a rotating cantilever beam with an adjusted proportional damping model. *Journal of Vibration Engineering and Technologies*, *13*(8), Article 599. https://doi.org/10.1007/s42417-025-02174-0.

7. Hamdi, H., Mrad, C., Hamdi, A., & Nasri, R. (2014). Dynamic response of a horizontal axis wind turbine blade under aerodynamic, gravity and gyroscopic effects. *Applied Acoustics*, *86*, 154–164. https://doi.org/10.1016/j.apacoust.2014.04.017.

8. Hodges, D.H., & Rutkowski, M.J. (1981). Free-vibration analysis of rotating beams by a variable-order finite-element method. *AIAA Journal*, *19*(11), 1459–1466. https://doi.org/10.2514/3.60082.

9. Jureczko, M., Pawlak, M., & Mężyk, A. (2005). Optimisation of wind turbine blades. *Journal of Materials Processing Technology*, *167*(2–3), 463–471. https://doi.org/10.1016/j.jmatprotec.2005.06.055.

10. Kim, H., Yoo, H.H., & Chung, J. (2013). Dynamic model for free vibration and response analysis of rotating beams. *Journal of Sound and Vibration*, *332*(22), 5917–5928. https://doi.org/10.1016/j.jsv.2013.06.004.

11. Lee, S.H., Shin, S.H., & Yoo, H.H. (2004). Flapwise bending vibration analysis of rotating composite cantilever beams. *KSME International Journal*, *18*(2), 240–245. https://doi.org/10.1007/BF03184733.

12. Leissa, A.W., Lee, J.K., & Wang, A.J. (1982). Rotating blade vibration analysis using shells. *Journal of Engineering for Gas Turbines and Power*, *104*(2), 296–302. https://doi.org/10.1115/1.3227279.

13. Maktouf, R., Yangui, M., Fakhfekh, T., Nasri, R., & Haddar, M. (2019). Non-linear dynamic analysis of a wind turbine blade. *Journal of the Chinese Institute of Engineers*, *42*(8), 727–737. https://doi.org/10.1080/02533839.2019.1660229.

14. Moeenfard, H., & Awtar, S. (2014). Modeling geometric nonlinearities in the free vibration of a planar beam flexure with a tip mass. *Journal of Mechanical Design*, *136*(4), Article 044502. https://doi.org/10.1115/1.4026147.

15. Ni, P., Xia, Y., Li, J., & Hao, H. (2019). Using polynomial chaos expansion for uncertainty and sensitivity analysis of bridge structures. *Mechanical Systems and Signal Processing*, *119*, 293–311. https://doi.org/10.1016/j.ymssp.2018.09.029

16. Pagani, A., & Carrera, E. (2018). Unified formulation of geometrically nonlinear refined beam theories. *Mechanics of Advanced Materials and Structures*, *25*(1), 15–31. https://doi.org/10.1080/15376494.2016.1232458.

17. Palacios, R., & Cesnik, S. (2009). Structural models for flight dynamic analysis of very flexible aircraft. In *50th AIAA/ASME/ASCE/AHS/ASC Structures, Structural Dynamics, and Materials Conference (AIAA 2009–2403). American Institute of Aeronautics and Astronautics*. https://doi.org/10.2514/6.2009-2403.

18. Park, J.-H., Park, H.-Y., Jeong, S.-Y., Lee, S.-I., Shin, Y.-H., & Park, J.-P. (2010). Linear vibration analysis of rotating wind-turbine blade. *Current Applied Physics*, *10*(2), S332–S334. https://doi.org/10.1016/j.cap.2009.11.036.

19. Schwarz, S., Carta, D., Monti, A., & Benigni, A. (2024). A direct and analytical method for inverse problems under uncertainty in energy system design: combining inverse simulation and Polynomial Chaos theory. *Energy Informatics*, *7*, Article 55. https://doi.org/10.1186/s42162-024-00360-0.

20. Serra, Q., & Florentin, E. (2023). Verification of polynomial chaos surrogates in the framework of structural vibrations with uncertainties. *Mechanics and Industry*, *24*, Article 42. https://doi.org/10.1051/meca/2023037.

21. Sheibani, M., & Akbari, A.A. (2015). Finite element modeling of a wind turbine blade. *Journal of Vibroengineering*, *17*(7), 3774–3791. https://doi.org/10.21595/jve.2015.16033

22. Yangui, M., Bouaziz, S., Taktak, M., Haddar, M., & El-Sabbagh, A. (2018). Nonlinear analysis of twisted wind turbine blade. *Journal of Mechanics*, *34*(3), 269–278. https://doi.org/10.1017/jmech.2016.120.

23. Zhang, P., & Huang, S. (2011). Review of aeroelasticity for wind turbine: Current status, research focus and future perspectives. *Frontiers in Energy*, *5*(4), 419–434. https://doi.org/10.1007/s11708-011-0166-6.

24. Zhao, Z., Wang, L., Li, X., & Wang, T. (2025). An efficient and high-precision nonlinear co-rotational beam method for wind turbine blades considering tapering effects and anisotropy. *Energies*, *18*(18), Article 4907. https://doi.org/10.3390/en18184907.

Manuscript received April 25, 2026; accepted for publication July 15, 2026;
published online July 22, 2026.